Research Article

JOURNAL OF CHEMOMETRICS

Received: 23 January 2009, Revised: 29 June 2009, Accepted: 11 August 2009, Published online in Wiley InterScience: 2009

(www.interscience.wiley.com) DOI: 10.1002/cem.1257

Blind decomposition of low-dimensional multi-spectral image by sparse component analysis

Ivica Kopriva[a]* and Andrzej Cichocki[b,c]

A multilayer hierarchical alternating least square nonnegative matrix factorization approach has been applied to blind decomposition of low-dimensional multi-spectral image. The method performs blind decomposition exploiting spectral diversity and spatial sparsity between materials present in the image and, unlike many blind source separation methods, is invariant with respect to statistical (in)dependence among spatial distributions of the materials. As opposed to many existing blind source separation algorithms, the method is capable of estimating the unknown number of materials present in the image. This number can be less than, equal to, or greater than the number of spectral bands. The method is validated on underdetermined blind source separation problems associated with blind decomposition of experimental red-green-blue images composed of four materials. Achieved performance has been superior when compared against methods based on minimization of the ℓ_1-norm: linear programming and interior-point methods. In addition to tumor demarcation, as demonstrated in the paper, other areas that can also benefit from the proposed method include cell, chemical, and tissue imaging. Copyright © 2009 John Wiley & Sons, Ltd.

Keywords: multi-spectral imaging; chemical imaging; cell imaging; sparse component analysis; nonnegative matrix factorization

1. INTRODUCTION

Due to the variety of potential civilian and military applications, blind decomposition of multi-spectral and hyper-spectral images has drawn considerable attention in recent years [1–8]. Owing to the fact that more than one material is expected to be present in each pixel footprint, blind multi-spectral image decomposition is a blind source separation (BSS) problem. A standard tool for the solution of the BSS problems is independent component analysis (ICA) [9–13], which is based on the assumption that materials are mutually statistically independent. However, as shown in Reference [14], this assumption is not fulfilled for the hyper-spectral and multi-spectral data due to the fact that the sum of the materials present in the pixel footprint must be constant [15]. Thus, materials must necessarily be statistically related. ICA also requires the unknown number of materials present in the image to be less than or equal to the number of spectral bands. This assumption is easily satisfied in the case of hyper-spectral imaging but is problematic when low-dimensional multi-spectral images are considered. Therefore, we propose an algorithm for blind decomposition of the low-dimensional multi-spectral images. Its performance does not depend on statistical relations among materials. The algorithm exploits spectral diversity of the materials present in the image as well as sparsity between their spatial distributions. The sparsity assumption implies that only a small number of materials occupies the pixel footprint. This constraint is necessary to narrow down the infinite number of factorizations that satisfy the linear mixture model of the multi-spectral image (defined in Section 2). Methods that solve BSS problems based on sparseness assumption are known as sparse component analysis (SCA) [16–18,41,42]. They solve related BSS problems in two phases: using a data clustering algorithm to estimate the mixing matrix and using ℓ_1-norm minimization to estimate spatial distributions of the materials present in the image. Geometrical methods proposed in Reference [15,19] for non-negative BSS problems cannot solve underdetermined BSS problems. This is in principle also true for nonnegative matrix and tensor factorization (NMF/NTF) methods [20–25], which exhibited poor performance in solving underdetermined BSS problems. This limitation has been alleviated recently through the introduction of the local or hierarchical NMF algorithm [23,25]. It sequentially minimizes local cost functions in the source recovery process. Because it employs alternating least squares minimization to estimate mixing matrix and matrix of the materials it has been coined the HALS NMF algorithm. When employed in a multilayer mode [26], the HALS NMF algorithm has demonstrated good performance in solving underdetermined BSS problems. Thus, the multilayer HALS NMF algorithm and its

* *Correspondence to: I. Kopriva, Division of Laser and Atomic Research and Development, Ruđer Bošković Institute, Bijenička cesta 54, HR-10000, Zagreb, Croatia.*
E-mail: ikopriva@irb.hr

a *I. Kopriva*
Division of Laser and Atomic Research and Development, Ruđer Bošković Institute, Bijenička cesta 54, HR-10000, Zagreb, Croatia

b *A. Cichocki*
Laboratory for Advanced Brain Signal Processing, Brain Science Institute, RIKEN 2-1Hirosawa, Wako-shi, Saitama, 351-0198, Japan

c *A. Cichocki*
Warsaw University of Technology and Systems Research Institute, PAN, Poland

application in blind multi-spectral image decomposition represent the main contributions of this paper. More details about this algorithm are presented in Section 3. Its capability to solve underdetermined BSS problem is demonstrated in Section 4 on challenging problems of blind decomposition of experimental red-green-blue (RGB) images. Very few algorithms exist for solving the blind multi-spectral image decomposition problem in underdetermined BSS scenario.

The rest of the paper is organized as follows. Section 2 introduces the static linear mixture model of the multi-spectral image. Section 3 presents HALS NMF (SCA)-based approach to blind multi-spectral image decomposition. Section 4 presents results of comparative performance analysis between multilayer HALS NMF algorithm and linear programming and interior point based ℓ_1-norm minimization methods. Conclusions are given in Section 5.

2. STATIC LINEAR MIXTURE MODEL OF THE MULTI-SPECTRAL IMAGE

Multi-spectral image is represented in a form of the static linear mixture model [1–6]:

$$\mathbf{X} = \mathbf{AS} \tag{1}$$

where $\mathbf{X} \in \mathbf{R}_{0+}^{N\times T}$ represents multi-spectral image consisting of N spectral bands and $T = P \times Q$ pixels, $\mathbf{A} \in \mathbf{R}_{0+}^{N\times M}$ represents mixing matrix or matrix of spectral responses, and $\mathbf{S} \in \mathbf{R}_{0+}^{M\times T}$ represents matrix of the M materials present in the image scene. Each row of $\mathbf{X}$ and $\mathbf{S}$ is a 1D image representation obtained from corresponding spectral image by some 2D→1D mapping called vectorization. Because we are concerned with an unsupervised image decomposition problem $\mathbf{X}$, $\mathbf{A}$, and $\mathbf{S}$ are assumed to be nonnegative.

Unsupervised decomposition of the linear mixture model (1) is a challenging BSS problem because both mixing matrix $\mathbf{A}$ and materials matrix $\mathbf{S}$ must be estimated having at disposal multi-spectral image matrix $\mathbf{X}$ only. Many BSS problems are efficiently solved by ICA [9–13] assuming materials $\{\mathbf{s}_m\}_{m=1}^{M}$ to be statistically independent and non-Gaussian as well as that the number of materials M is less than or equal to the number of spectral bands N. As discussed in the introduction, these assumptions are not fulfilled in a low-dimensional multi-spectral imaging scenario. In such a scenario estimating the number of materials M is a challenging problem as well. Many approaches based the on ranking of the singular values of the sample data covariance matrix $\mathbf{R}_{\mathbf{X}} \approx \mathbf{X}\mathbf{X}^{\mathrm{T}}$ [27–29] cannot be used, because the number of singular values N is less than the number of materials M. In the proposed HALS NMF algorithm we treat M as an unknown variable that is estimated together with the mixing matrix $\mathbf{A}$ by the to be described data clustering algorithm [18].

3. SCA-BASED BLIND MULTI-SPECTRAL IMAGE DECOMPOSITION

When the linear system of Equation (1) is underdetermined the null space of $\mathbf{A}$ is nontrivial. Thus, the inverse problem has many solutions and additional constraints such as sparseness between the components of the column vectors $\{\mathbf{s}(t)\}_{t=1}^{T}$ are necessary to narrow down the number of solutions. The SCA concept is used to find a good approximation of the true solution to an underdetermined system of linear equations subject to sparsity constraints. A sparse signal is a signal with just few per cent of the samples that are nonzero. Signal that has at least $k \leq M$ nonzero components is called k-sparse. The SCA is carried out using the two following approaches. The first one employs NMF algorithms, where mixing matrix $\mathbf{A}$ and source matrix $\mathbf{S}$ are estimated simultaneously. This is achieved usually through alternating least square methodology [22–25]. The second one referred in Reference [17,18,30–32] breaks down BSS problem into two separate problems: estimation of the mixing matrix $\mathbf{A}$ and the number of materials M using the geometric concept known as data clustering [15,17,18,30–32] and estimation of the materials or source matrix $\mathbf{S}$ (based on estimated $\mathbf{A}$) by solving resulting underdetermined system of linear equations. This last step is carried out as linear programming [16,30,31,32], ℓ_1-regularized least square problem [33,34], or ℓ_2-regularized linear problem [35].

To solve underdetermined BSS problems, the majority of clustering algorithms require that signal $\{\mathbf{s}(t)\}_{t=1}^{T}$ is $(N-1)$-sparse with M-N+1 zero components. By setting the number of mixtures to be $N = 3$ (this corresponds with an RGB image) this implies $k = 2$. It means that only two materials in the RGB image are allowed to occupy each pixel footprint. However, in the blind multi-spectral image decomposition problem considered in this paper we shall assume that materials present in the image are on average $k = 1$ sparse. This implies that at each pixel footprint in average only one material is present. This assumption allows the reduction of the computational complexity of the data clustering algorithm [18]. It is, however, a correct assumption in the considered problem of medical imaging of the skin tumors [8,36]. There, due to the small field of view the pixel footprint is very small (significantly less than 1 mm^2). Thus, it is not reasonable to expect that more than one material will occupy such a small area (for example see experimental RGB images of the skin tumor shown in Figures 5 and 7).

3.1. Multilayer HALS NMF algorithm

The HALS NMF algorithm minimizes global cost function to estimate mixing matrix $\mathbf{A}$ and set of local cost functions to estimate the unknown materials $\{\underline{\mathbf{s}}_m\}_{m=1}^{M}$. Global cost function employed for the estimation of the mixing matrix is

$$D(\mathbf{X}\|\mathbf{AS}) = \frac{1}{2}\|\mathbf{X} - \mathbf{AS}\|_2^2 + \alpha_S J_S(\mathbf{S}) + \alpha_A J_A(\mathbf{A}) \tag{2}$$

where $J_{\mathbf{S}}(\mathbf{S})$ and $J_{\mathbf{A}}(\mathbf{A})$ represent sparseness constraint and $\alpha_{\mathbf{S}}$ and $\alpha_{\mathbf{A}}$ represent corresponding regularization constants. Because no constraints are imposed on $\mathbf{A}$ and because cost function (2) is minimized with respect to $\mathbf{A}$ only, both regularization constants in Equation (2) are set to zero, i.e., $\alpha_{\mathbf{S}} = \alpha_{\mathbf{A}} = 0$. To estimate matrix of materials $\mathbf{S}$ we employ minimization of the local cost functions [23,25]:

$$\begin{aligned} &D^{(m)}\left(\mathbf{X}^{(m)}\|\mathbf{a}_m\underline{\mathbf{s}}_m\right) \\ &= \frac{1}{2}\left\|\mathbf{X}^{(m)} - \mathbf{a}_m\underline{\mathbf{s}}_m\right\|_2^2 + \alpha_s^{(m)} J_S(\underline{\mathbf{s}}_m) + \alpha_a^{(m)} J_a(\mathbf{a}_m) \\ &m = 1, \ldots, M \end{aligned} \tag{3}$$

where $\mathbf{a}_m$ represents columns of $\mathbf{A}$ and $\underline{\mathbf{s}}_m$ represents rows of $\mathbf{S}$ and $\mathbf{X}^{(m)} = \mathbf{X} - \sum_{j\neq m}\mathbf{a}_j\underline{\mathbf{s}}_j$. Because no constraints are imposed on $\mathbf{A}$ we set $\alpha_{\mathbf{a}}^{(m)} = 0$. Since in the considered blind multi-spectral image decomposition problem we have also assumed that materials on average do not overlap in spatial

domain, the sparseness constraint is imposed on them: $J_{\mathbf{S}}(\underline{\mathbf{s}}_m) = \sum_{t=1}^{T} s_{mt}$, where $\alpha_s^{(m)}$ is a regularization constant. Local learning rule for rows of **S** and global learning rule for **A** is finally obtained as

$$\begin{aligned} &\left\{ \underline{\mathbf{s}}_m \leftarrow \left[\mathbf{a}_m^T \mathbf{X}^{(m)} - \alpha_s^{(m)} \mathbf{1}_{1\times T} \right]_+ \right\}_{m=1}^{M} \\ &\mathbf{A} \leftarrow \left[\mathbf{X}\mathbf{S}^T \left(\mathbf{S}\mathbf{S}^T + \lambda \mathbf{I}_M \right)^{-1} \right]_+ \\ &\left\{ \mathbf{a}_m \leftarrow \mathbf{a}_m / \|\mathbf{a}_m\|_2 \right\}_{m=1}^{M} \end{aligned} \tag{4}$$

where $\mathbf{I}_M$ is an $M \times M$ identity matrix, $\mathbf{1}_{1\times T}$ is a row vector with all entries equal to 1, and $[\xi]_+ = \max\{\varepsilon, \xi\}$ (e.g., $\varepsilon = 10^{-16}$). Regularization constant λ changes as a function of the iteration index as: $\lambda_k = \lambda_0 \exp(-k/\tau)$ (with $\lambda_0 = 20$ and $\tau = 0.002$ in the experiments). ALS concept implies that cost functions (3) and (4) are minimized in an alternating fashion. Significant improvement in the performance of the NMF algorithms is obtained when they are applied in the multilayer mode [26], whereas sequential decomposition of the nonnegative matrices is performed as follows. In the first layer, the basic approximation decomposition is performed $\mathbf{X} \cong \mathbf{A}^{(1)}\mathbf{S}^{(1)} \in \mathbf{R}_{0+}^{N\times T}$. In the second layer the result from the first layer is used to build up a new input data matrix for the second layer $\mathbf{X} \leftarrow \mathbf{S}^{(1)} \in \mathbf{R}_{0+}^{M\times T}$ yielding $\mathbf{X}^{(1)} \cong \mathbf{A}^{(2)}\mathbf{S}^{(2)} \in \mathbf{R}_{0+}^{M\times T}$. After L layers, the data decompose as follows:

$$\mathbf{X} \cong \mathbf{A}^{(1)}\mathbf{A}^{(2)} \cdots \mathbf{A}^{(L)}\mathbf{S}^{(L)} \tag{5}$$

Thus, learning rules (4) combined with the multilayer mode of operation (5) is what constitutes the multilayer HALS NMF algorithm.

3.2. ℓ_1-norm minimization algorithms

Presuming the mixing matrix **A** is estimated through the data clustering algorithm, materials can also be estimated by means of linear programming

$$\begin{aligned} &\hat{\mathbf{s}}(t) = \arg\min_{\mathbf{s}(t)} \sum_{m=1}^{\hat{M}} s_m(t) \text{ subject to } \hat{\mathbf{A}}\mathbf{s}(t) = \mathbf{x}(t) \\ &\forall t = 1, \ldots, T \end{aligned} \tag{6}$$

If the noise is present in the blind decomposition problem more robust solution for $\{\mathbf{s}(t)\}_{t=1}^{T}$ is obtained by solving the ℓ_1-regularized least square problem [33,34]:

$$\begin{aligned} &\hat{\mathbf{s}}(t) = \arg\min_{\mathbf{s}(t)} \frac{1}{2} \left\| \hat{\mathbf{A}}\mathbf{s}(t) - \mathbf{x}(t) \right\|_2^2 + \lambda \|\mathbf{s}(t)\|_1 \\ &\forall t = 1, \ldots, T \end{aligned} \tag{7}$$

or the ℓ_2-regularized linear problem [35]:

$$\begin{aligned} &\hat{\mathbf{s}}(t) = \arg\min_{\mathbf{s}(t)} \|\mathbf{s}(t)\|_1 \text{ subject to } \left\| \hat{\mathbf{A}}\mathbf{s}(t) - \mathbf{x}(t) \right\|_2^2 \le \varepsilon \\ &\forall t = 1, \ldots, T \end{aligned} \tag{8}$$

Note that all three formulations, (6–8), employed to solve the resulting underdetermined system of linear equations are carried out on the pixel level. Hence, they are well suited for massively parallel implementation. Similarly, the clustering algorithm to be described could also be parallelized by applying it on several disjoint pixel regions and then merging clustering results.

3.3. Data clustering algorithm

The importance of data clustering for the HALS NMF algorithm and ℓ_1-norm minimization algorithms is very different. In the former case, it is only important for estimating the number of materials present in the image. In the latter case, it is also important for estimating the mixing matrix that is necessary for the solution of problems (6–8). Thus, the final performance of blind image decomposition will be much more dependent on the accuracy of data clustering when the ℓ_1-norm minimization algorithms are employed than when the HALS NMF algorithm is employed. This is an additional argument to advocate the use of the HALS NMF algorithm in blind multi-spectral image decomposition.

Because the solution of the BSS problem is generally characterized by scale indeterminacy we shall assume the unit norm constraint (in the sense of ℓ_2 norm) on the columns of the mixing matrix **A**, i.e., $\left\{ \|\mathbf{a}_m\|_2 = 1 \right\}_{m=1}^{M}$. Since we have assumed the number of mixtures to be $N = 3$, the normalized mixing vectors $\{\mathbf{a}_m\}_{m=1}^{M}$ lie in a 3D space on the unit semi-sphere. They are parameterized as

$$\mathbf{a}_m = [\cos(\varphi_m)\sin(\theta_m) \;\; \sin(\varphi_m)\sin(\theta_m) \;\; \cos(\theta_m)]^T \tag{9}$$

where φ_m and θ_m represent azimuth and elevation angles respectively. Due to the nature of the problem coefficients of the mixing vectors are nonnegative. Consequently, the mixing angles φ_m and θ_m are confined in the interval $[0, \pi/2]$.

By assuming *1*-dimensional concentration subspaces the clustering algorithm is outlined by the following steps:

(1) We remove all data points close to the origin for which $\left\{ \|\mathbf{x}(t)\|_2 \le \varepsilon \right\}_{t=1}^{T}$ is applicable, where ε represents some predefined threshold. This corresponds to the case when all materials are close to zero.

(2) Normalize to unit ℓ_2 norm remaining data points $\mathbf{x}(t)$, i.e., $\left\{ \mathbf{x}(t) \leftarrow \mathbf{x}(t) / \|\mathbf{x}(t)\|_2 \right\}_{t=1}^{\overline{T}}$, where $\overline{T} \le T$ denotes the number of data points that remained after the elimination process.

(3) Calculate function $f(\mathbf{a})$, where **a** is defined with Equation (9):

$$f(\mathbf{a}) = \sum_{t=1}^{\overline{T}} \exp\left(-\frac{d^2(\mathbf{x}(t), \mathbf{a})}{2\sigma^2} \right) \tag{10}$$

where $d(\mathbf{x}(t), \mathbf{a}) = \sqrt{1 - (\mathbf{x}(t) \cdot \mathbf{a})^2}$ and $(\mathbf{x}(t) \cdot \mathbf{a})$ denotes inner product. Parameter σ in equation (10) is called dispersion. If set to sufficiently small value, in our experiments this turned out to be $\sigma \approx 0.05$, the value of the function $f(\mathbf{a})$ will approximately equal the number of data points close to **a**. Thus, by varying mixing angles $0 \le \varphi, \theta \le \pi/2$ we effectively cluster data.

(4) Number of peaks of the function $f(\mathbf{a})$ corresponds with the estimate of the number of materials $\hat{M}$. Locations of the peaks correspond with the estimates of the mixing angles $\left\{ (\hat{\varphi}_m, \hat{\theta}_m) \right\}_{m=1}^{\hat{M}}$, i.e., mixing vectors $\left\{ \hat{\mathbf{a}}_m \right\}_{m=1}^{\hat{M}}$, where $\hat{\mathbf{a}}_m$ is given with equation (9). The hat sign introduced here is used to denote the estimate of the related quantity. Hence, at the end of data clustering phase estimates of the number of materials $\hat{M}$ and mixing matrix **A** are obtained.

From the above exposition, it is evident that the value of dispersion constant σ in (10) will influence the number of clusters. Therefore, in real world situations the number of clusters will most likely be either over- or underestimated. Practical experience with certain type of data sets will help in the proper selection of the parameter σ. Generally, if the number of clusters is

underestimated, spectrally similar materials will be extracted (segmented) together as one material. If the number of clusters is overestimated some materials will be extracted several times. This latter case is less dangerous than the former one, because in the former case some materials are lost. The existence of multiple materials is checked easily by calculating how much they are mutually correlated. Thus, one way to circumvent the difficulty associated with the under- or overestimation of the number of clusters is to run the algorithm twice with two different values of dispersion constant σ and check whether new mutually uncorrelated spatial maps will be extracted or some of the extracted maps will be repeated.

4. EXPERIMENTAL RESULTS

Two examples related to the blind decomposition of experimental RGB images are used for comparative performance analysis between: multilayer HALS NMF algorithm (4) and (5) [23,26], linear programming method used to solve problem (6), and interior-point method [33] used to solve problem (7). The principal reason for using RGB images and not hyperspectral images for performance evaluation is that the underdetermined BSS problem is very likely to occur in this low-dimensional multispectral case. Linear programming algorithm is implemented by MATLAB command linprog, while MATLAB code for interior-point method has been provided in Reference [37]. To cope with the eventual presence of noise in the experimental RGB image regularization constant in Equation (7) was set to $\lambda = 10$. This is due to the fact that the optimal value of the regularization constant is proportional to the noise variance [38,39]. Both examples were implemented in MATLAB environment on 2.4 GHz Intel Core 2 Quad Processor Q6600 based desktop computer with 4 GB RAM.

4.1. Experiment 1: RGB image consisting of four materials

Blind decomposition of the experimental RGB image shown in Figure 1 that consists of four materials is an underdetermined BSS problem. Because materials in the experimental RGB image do not overlap in spatial domain, we can evaluate the performance of the employed blind image decomposition methods via the correlation matrix defined as $\mathbf{G} = \mathbf{S}\mathbf{S}^{\mathrm{T}}$. For the perfect separation the correlation matrix should be diagonal. Hence, separation performance can be visualized as a deviation from the diagonal matrix (see Figure 4). To quantify decomposition quality numerically we compute the correlation index in dB scale as

$$CR = -10 \log_{10} \sum_{\substack{i,j=1 \\ j \neq i}}^{M} g_{ij}^2 \tag{11}$$

where before calculating the correlation matrix $\mathbf{G}$ rows of $\mathbf{S}$ are normalized to unit ℓ_2 norm. To make the extracted spatial maps of the materials visually comparable, we have rescaled each extracted material to the interval [0, 1], wherein 0 represents the absence of the material and 1 represents the presence of the material. Hence, the quality of the image decomposition is visible immediately. Figure 2 shows the clustering function, Equation (10), in the domain of mixing angles with the dispersion constant $\sigma = 0.05$. Four clusters confirm the existence of four materials present in the RGB image.

Multilayer HALS NMF algorithm [23,26], with the sparseness regularization constraint $\alpha_s^{(m)} = 0.5$, 25 layers, and 500 iterations per layer has been applied to perform the blind image decomposition task. Figure 3 shows decomposition results obtained by the multilayer HALS NMF algorithm, interior point method, and linear programming method. Corresponding correlation matrices are shown in Figure 4. Numerical values of the correlation index in dB and computation times in seconds are given in Table I. The multilayer HALS NMF algorithm outperformed the other two SCA approaches in terms of the separation quality keeping at the same time the same level of computational complexity. The size of the RGB image shown in Figure 1 was $T = 384 \times 512 = 196608$ pixels. Computation times are estimated only for the multilayer HALS NMF algorithm (4) and (5), interior-point method employed to solve (7), and linear program employed to solve (6). The computation time of data clustering algorithm [18] was not taken into account because all three SCA algorithms under consideration used results of data clustering algorithm for their inputs. Thus, the data clustering method contributed to the computational complexity of all three methods equally.

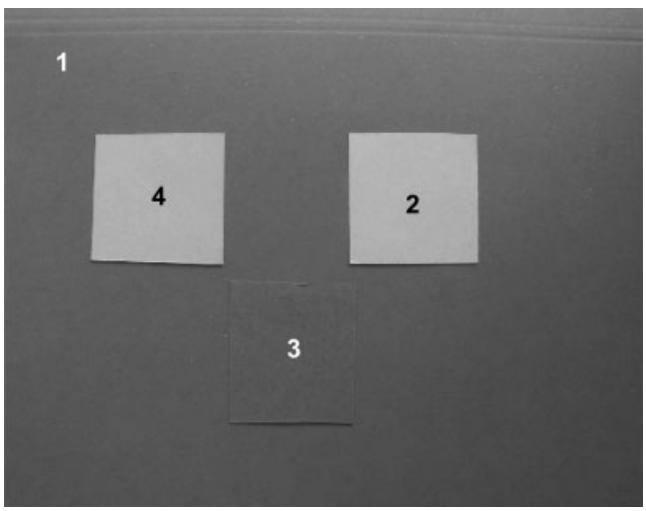

Figure 1. Experimental RGB image consisted of four different materials 1 to 4.

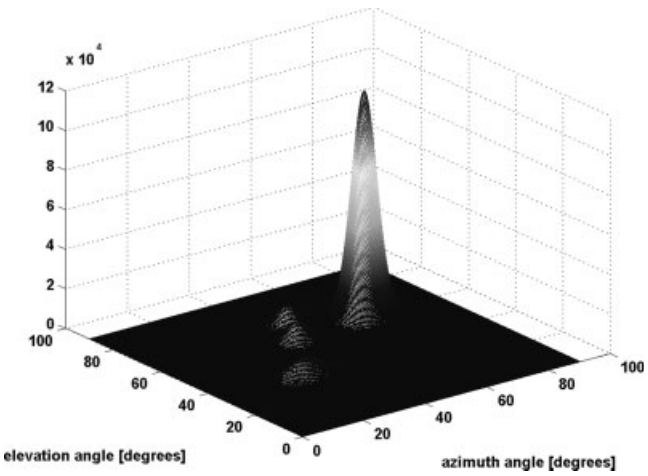

Figure 2. Clustering function (10) in the domain of mixing angles for the RGB image shown in Figure 1. Dispersion constant was $\sigma = 0.05$. Four clusters confirm the existence of the four materials in the RGB image.

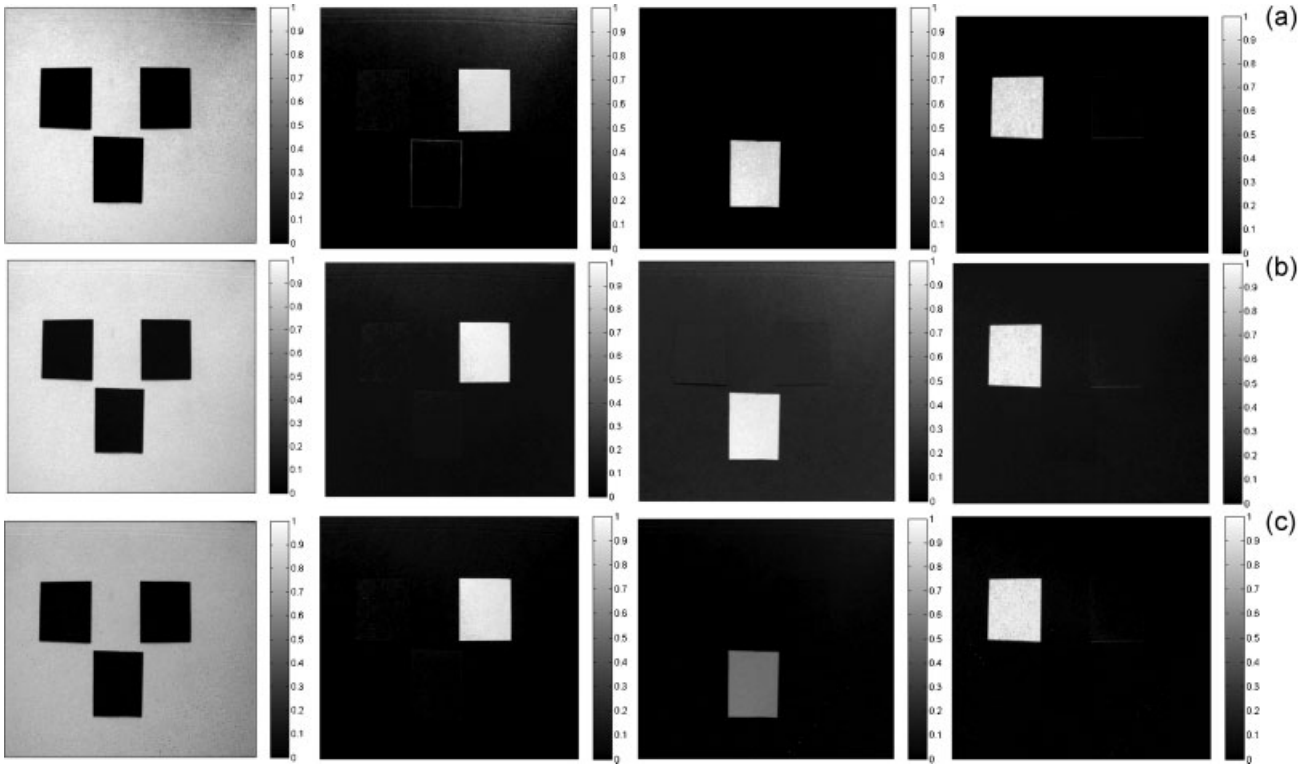

Figure 3. Spatial maps of the materials extracted from the RGB image shown in Figure 1 by means of: a) multilayer HALS NMF algorithm [23–26] with 25 layers, 500 iterations per layer, and sparseness constraints $\alpha_s^{(m)} = 0.5$; b) interior point method [33, 37]; c) linear programming. Extracted materials were rescaled to the interval [0, 1], wherein 0 represents the absence of the material and 1 represents the presence of the material.

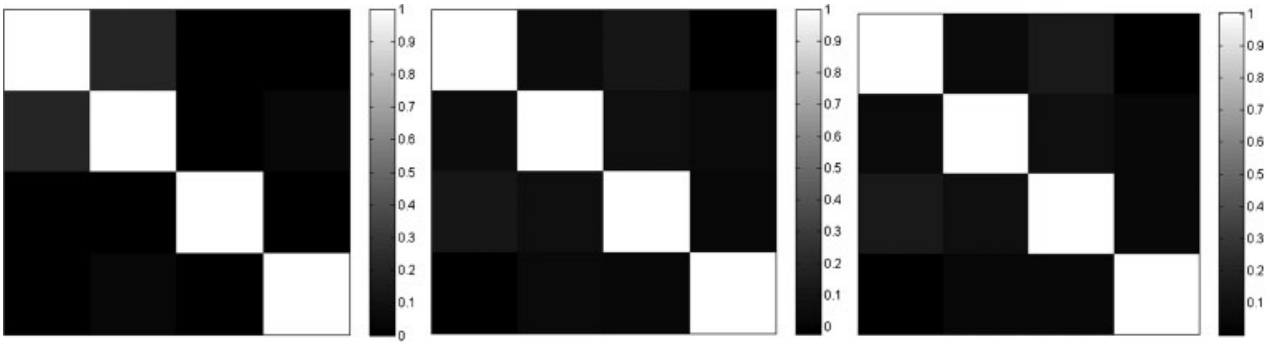

Figure 4. Correlation maps of the extracted sources. From left to right: multilayer HALS NMF algorithm [23–26] with 25 layers, 500 iterations per layer and sparseness constraints $\alpha_s^{(m)} = 0.5$, interior point method [33,37], and linear programming.

Table I. Rows: CR performance, Equation (11), and computational time for: multilayer HALS NMF algorithm, [23,26]; ℓ_1-regularized least square problem, [33,37]; linear programming. Columns: Type of algorithm employed to solve blind RGB image decomposition problem

	Multilayer HALS NMF (4) and (5)	Interior-point method (7)	Linear program (6)
CR (dB)	13.67	9.97	7.77
CPU time (s)	3097	7751	3265

4.2. Experiment 2: RGB fluorescent images of the skin tumor

We now execute the comparative performance evaluation of the presented methods on the RGB fluorescent image of the skin tumor (basal cell carcinoma) [36]. Other image processing methods widely used for the demarcation of the basal cell carcinoma include threshold based imaging [43] and ratio imaging [44]. However, as previously demonstrated in [8], the accuracy of these methods depends heavily on the optimality of the threshold parameter that is, to some extent, defined heuristically. For this purpose of tumor demarcation, an image of a skin tumor is recorded after the tumor was treated for 4 h with δ-5-aminolaevulinic acid (ALA). ALA is a photo-synthesizer that, through the process of biosynthesis, causes formation of the fluorophore protoporphyrin IX (PpIX) [40]. The tumor was

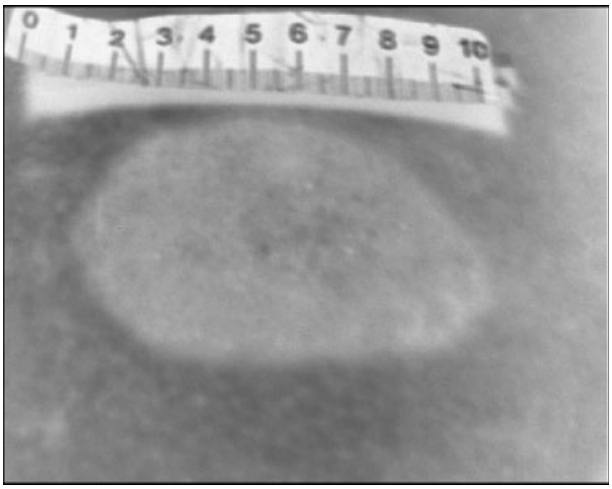

Figure 5. RGB fluorescent image of the skin tumor acquired after illumination with high-intensity light.

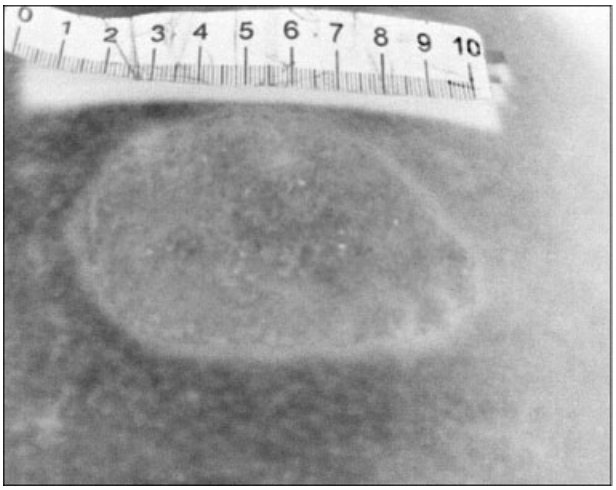

Figure 7. RGB fluorescent image of the skin tumor acquired after illumination with weak intensity light.

illuminated with 405 nm light, which induces fluorescence of the PpIX. The fluorescent image was recorded by a camera with an attached filter used to filter out the reflected 405 nm light. In order to evaluate the robustness of the image decomposition methods against the variation of the intensity of fluorescence, fluorescent RGB image of the tumor has been acquired after illumination with high-intensity light (shown in Figure 5) as well as after illumination with weak-intensity light (shown in Figure 7). The size of the images shown in Figures 5 and 7 was $T = 856 \times 1144 = 979264$ pixels. The high-intensity fluorescent image shown in Figure 5 was used to extract spatial binary maps of the tumor and surrounding healthy tissue. They served as a ground truth for the calculation of the receiver-operating-characteristic (ROC) curves necessary to quantify the performance of the SCA algorithms. Like in Figure 1, fluorescent RGB images shown in Figures 5 and 7 also contain four materials. They are: basal cell carcinoma, surrounding healthy tissue, the ruler that was inserted into the scene to give perspective about the spatial dimensions of the tumor and the border region between tumor and surrounding tissue that is spectrally distinct from both tumor and healthy tissue. Figure 6

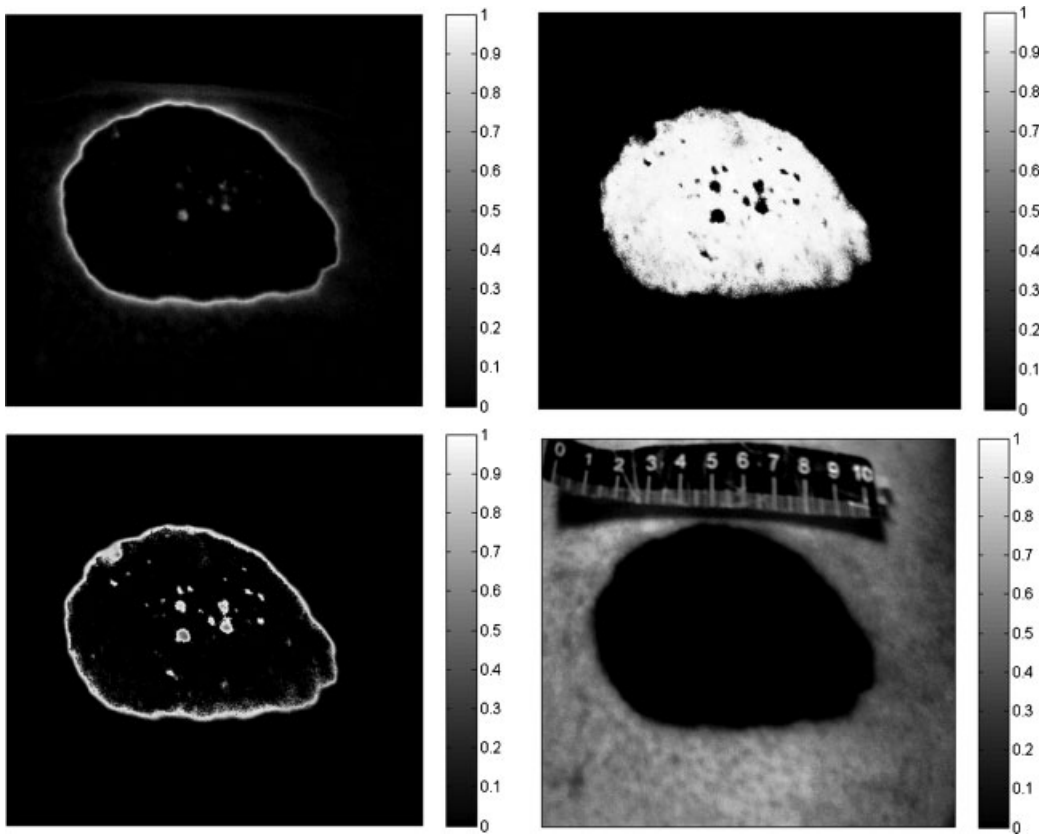

Figure 6. Spatial maps of the materials extracts from the fluorescent RGB image shown in Figure 5 by means of multilayer HALS NMF algorithm [23–26] with 25 layers, 500 iterations per layer, and sparseness constraints $\alpha_s^{(m)} = 0.5$.

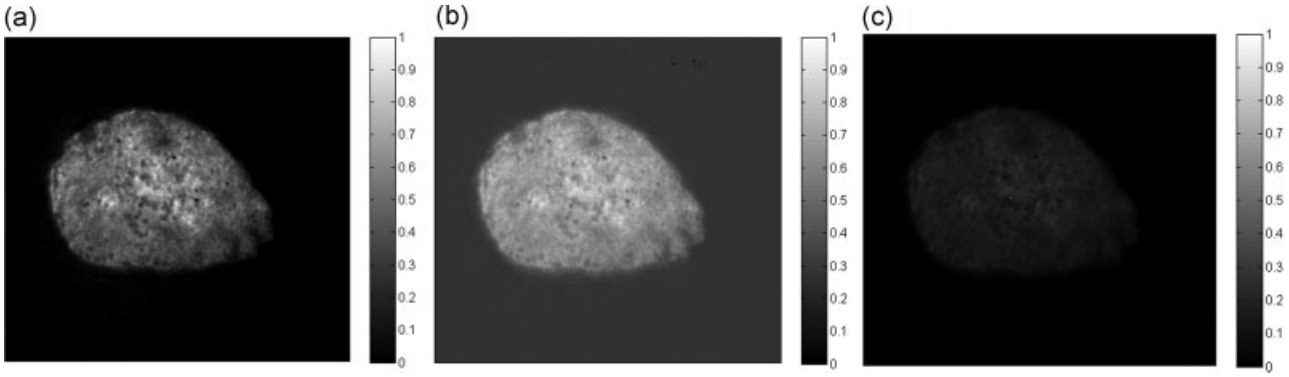

Figure 8. Spatial maps of the tumor extracted from the fluorescent RGB image shown in Figure 7. a) multilayer HALS NMF algorithm [23–26] with 5 layers, 1000 iterations per layer, and sparseness constraints $\alpha_s^{(m)} = 0.1$; b) interior point method [33,37]; c) linear programming. Extracted materials were rescaled to the interval [0, 1], wherein 0 represents the absence of the material and 1 represents the presence of the material.

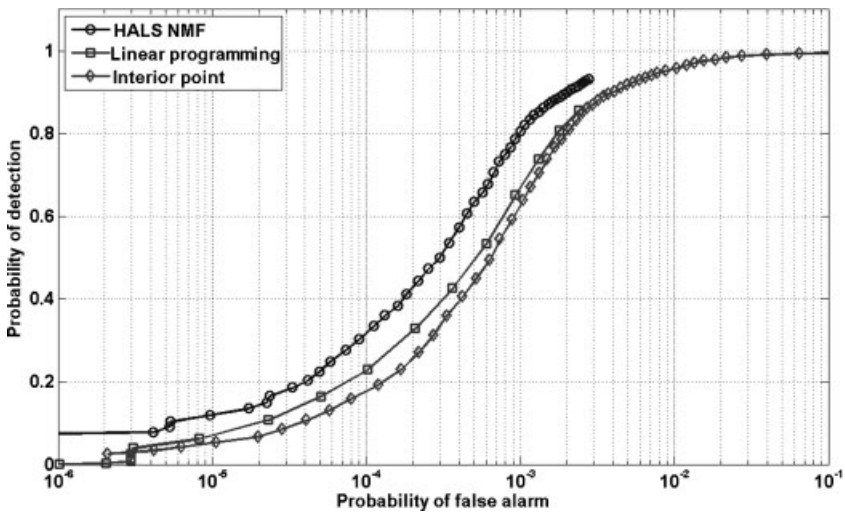

Figure 9. ROC curves calculated for spatial maps of the tumor shown in Figure 8 according to legend: circles—multilayer HALS NMF algorithm; squares—linear programming method; diamonds—interior point method.

shows spatial distributions of these materials extracted by the multilayer HALS NMF algorithm [23,26] with sparseness regularization constraint $\alpha_s^{(m)} = 0.5$, 25 layers, and 500 iterations per layer. Like in example 4.1, extracted spatial maps are rescaled to the interval [0, 1], wherein 0 represents the absence of the material and 1 represents the presence of the material. The image in the upper right corner of Figure 6 represents the spatial map of the basal cell carcinoma. All four extracted spatial maps have meaningful interpretation and are consistent with our knowledge of the structure of the RGB image shown in Figure 5. Extraction of the tumor spatial map with the stable boundary from the low-intensity fluorescent image (shown in Figure 7) was a challenge for blind decomposition methods. Figures 8a to 8c, respectively, show spatial maps of the tumor extracted from the RGB image shown in Figure 7 by means of: multilayer HALS NMF algorithm (4) and (5) with sparseness regularization constraint $\alpha_s^{(m)} = 0.1$, 5 layers, and 1000 iterations per layer; interior point method (7) and linear programming method (6). The multilayer HALS NMF algorithm yielded significantly larger separation margin between the tumor material and the rest of the image than other two methods. This is confirmed in Figure 9 which shows ROC curves for the three methods. For the same probability of false alarm, the HALS NMF algorithm yields greater probability of detection.

5. CONCLUSION

Multilayer hierarchical alternating least square nonnegative matrix factorization algorithm is proposed for the blind decomposition of low-dimensional multi-spectral image. Performance of the algorithm is invariant with respect to statistical (in)dependence among materials present in the image which is not the case with the majority of BSS methods. Unlike many other BSS methods, the proposed algorithm is capable of estimating the unknown number of materials present in the image as well as extracting spatial distributions of the materials when the number

of materials is greater than the number of spectral bands. The outlined capabilities have been experimentally demonstrated on RGB images with the known ground truth. It has been demonstrated quantitatively through comparative performance analysis that multilayer HALS NMF algorithm outperforms other state-of-the-art methods in solving underdetermined BSS problems: interior point method and linear programming method. In addition to the tumor demarcation problem that is demonstrated in the paper, other areas that can also benefit from the proposed method are cell and chemical imaging with application in chemistry, biology, and medicine.

Acknowledgements

This work was supported through grant 098-0982903-2558 funded by the Ministry of Science, Education and Sports, Republic of Croatia. The authors wish to thank anonymous reviewers for very constructive comments that contributed to the quality of the paper significantly. The authors also thank Ivanka Jerić and David Nagel for proofreading the final version of the manuscript.

REFERENCES

1. Adams JB, Smith MO. Spectral mixture modeling: a new analysis of rock and soil types at the Viking Lander 1 suite. *J. Geophys. Res.* 1986; **91**: 8098–8112.
2. Settle JJ, Drake NA. Linear mixing and estimation of ground cover proportions. *Int. J. Remote Sens.* 1993; **14**: 1159–1177.
3. Chang C-I, Chiang S-S, Smith JA, Ginsberg IW. Linear spectral random mixture analysis for hyperspectral imagery. *IEEE Trans. Geosci. Remote Sensing* 2002; **40**: 375–392.
4. Du Q, Kopriva I, Szu H. Independent-component analysis for hyperspectral remote sensing imagery classification. *Opt. Eng.* 2006; **45: 017008**: 1–13.
5. Du Q, Kopriva I. Automated target detection and discrimination using constrained kurtosis maximization. *IEEE Geosci. Remote Sens. Lett.* 2008; **5**: 38–42.
6. Stein DWJ, Beaven SG, Hoff LE, Winter EM, Schaum AP, Stocker AD. Anomaly detection from hyperspectral imagery. *IEEE Signal Process. Mag.* 2002; **19**: 58–69.
7. Zavattini G, Vecchi S, Mitchell G, Weisser U, Leahy RM, Pichler BJ, Smith DJ, Cherry SJ. A hyperspectral fluorescence system for 3D *in vivo* optical imaging. *Phys. Med. Biol.* 2006; **51**: 2029–2043.
8. Kopriva I, Peršin A, Zorc H, Lipozenčić J, Pašić A, Kostović K, Lončarić M. Visualization of basal cell carcinoma by fluorescence diagnosis and independent component analysis. *Photodiagnosis and Photodynamic Therapy* 2007; **4**: 190–196.
9. Hyvärinen A, Karhunen J, Oja E. *Independent Component Analysis*. John Wiley & Sons, Inc.: New York, US, 2001.
10. Cichocki A, Amari S. *Adaptive Blind Signal and Image Processing*. John Wiley: New York, 2002.
11. Jutten C, Herault J. Blind separation of sources, part I: an adaptive algorithm based on neuromimetic architecture. *Sig. Proc.* 1991; **24**: 1–10.
12. Comon P. Independent component analysis—a new concept? *Sig. Proc.* 1994; **36**: 287–314.
13. Cardoso JF, Soulomniac A. Blind beamforming for non-Gaussian signals. *Proc. IEE F* 1993; **140**: 362–370.
14. Nascimento JMP, Bioucas Dias JM. Does independent component analysis play a role in unmixing hyperspectral data? *IEEE Trans. Geosci. Remote Sensing* 2005; **43**: 175–187.
15. Nascimento JMP, Bioucas Dias JM. Vertex component analysis: a fast algorithm to unmix hyperspectral data. *IEEE Trans. Geosci. Remote Sensing* 2005; **43**: 898–910.
16. Li Y, Cichocki A, Amari S. Analysis of sparse representation and blind source separation. *Neural Comput.* 2004; **16**: 1193–1234.
17. Li Y, Amari S, Cichocki A, Ho DWC, Xie S. Underdetermined blind source separation based on sparse representation. *IEEE Trans. Signal Process.* 2006; **54**: 423–437.
18. Naini FM, Mohimani GH, Babaie-Zadeh M, Jutten C. Estimating the mixing matrix in sparse component analysis (SCA) based on partial *k*-dimensional subspace clustering. *Neurocomputing* 2008; **71**: 2330–2343.
19. Chan TH, Ma WK, Chi Ch Y, Wang Y. A convex analysis framework for blind separation of non-negative sources. *IEEE Trans. Signal Process.* 2008; **56**: 5120–5134.
20. Lee DD, Seung HS. Learning the parts of objects by non-negative matrix factorization. *Nature* 1999; **401**: 788–791.
21. Cichocki A, Zdunek R, Amari S. Nonnegative matrix and tensor factorization. *IEEE Signal Process. Mag.* 2008; **25**: 142–145.
22. Zdunek R, Cichocki A. Nonnegative matrix factorization with constrained second-order optimization. *Sig. Proc.* 2008; **87**: 1904–1916.
23. Cichocki A, Zdunek R, Amari SI. Hierarchical ALS algorithms for nonnegative matrix factorization and 3D tensor factorization. *LNCS* 2007; **4666**: 169–176.
24. Cichocki A, Phan A-H, Zdunek R, Zhang L-Q. Flexible component analysis for sparse, smooth, nonnagative coding or representation. *LNCS* 2008; **4984**: 811–820.
25. Cichocki A, Zdunek R, Phan AH, Amari S. *Nonnegative Matrix and Tensor Factorization*. John Wiley & Sons, Ltd: New York, US, 2009.
26. Cichocki A, Zdunek R. Multilayer nonnegative matrix factorization. *Electron. Lett.* 2006; **42**: 947–948.
27. Levina E, Wagaman AS, Callender AF, Mandair GS, Morris MD. Estimating the number of pure chemical components in a mixture by maximum likelihood. *J. Chemometr.* 2007; **21**: 24–34.
28. Malinowski ER. Determination of the number of factors and experimental error in a data matrix. *Anal. Chem.* 1977; **49**: 612–617.
29. Chang CI, Du Q. Estimation of number of spectrally distinct signal sources in hyperspectral imagery. *IEEE Trans. Geosci. Remote Sensing* 2004; **42**: 608–619.
30. Bofill P, Zibulevsky M. Underdetermined blind source separation using sparse representations. *Sig. Proc.* 2001; **81**: 2353–2362.
31. Takigawa I, Kudo M, Toyama J. Performance analysis of minimum l_1-norm solutions for underdetermined source separation. *IEEE Trans. Signal Process.* 2004; **52**: 582–591.
32. Donoho DL, Elad M. Optimally sparse representation in general (nonorthogonal) dictionaries via l_1 minimization. *Proc. Natl Acad. Sci. USA* 2003; **100**: 2197–2202.
33. Kim SJ, Koh K, Lustig M, Boyd S, Gorinevsky S. An interior-point method for large-scale ℓ_1-regularized least squares. *IEEE J. Selected Topics Sig. Proc.* 2007; **1**: 606–617.
34. Tropp JA, Gilbert AC. Signal recovery from random measurements via orthogonal matching pursuit. *IEEE Trans. Inf. Theory* 2007; **53**: 4655–4666.
35. Figuiredo MAT, Nowak RD, Wright SJ. Gradient projection for sparse reconstruction: application to compressed sensing and other inverse problems. *IEEE J. Selected Topics Sig. Proc.* 2007; **1**: 586–597.
36. Kopriva I, Peršin A. Unsupervised decomposition of low-intensity low-dimensional multi-spectral fluorescent images for tumour demarcation. *Med. Image Anal.* 2009; **13**: 507–518.
37. http://www.stanford.edu/∼boyd/l1_ls/
38. Van Den Berg E, Friedlander MP. Probing the pareto frontier for basis pursuit solutions. *SIAM J. Sci. Comput.* 2008; **31**: 890–912.
39. Chen S, Donoho D, Saounders M. Atomic decomposition by basis pursuit. *SIAM J. Sci. Comput.* 1998; **20**: 33–61.
40. Koenig F, Knittel J, Stepp H. Diagnostic cancer in vivo. *Science* 2001; **292**: 1401–1403.
41. Luengo D, Santamaria I, Vielva L. A general solution to blind inverse problems for sparse input signal. *Neurocomputing* 2005; **69**: 198–215.
42. Georgiev P, Theis F, Cichocki A. Sparse component analysis and blind source separation of underdetermined mixtures. *IEEE Trans. Neural Netw.* 2005; **16**: 992–996.
43. Ericson MB, Sandberg C, Gudmundson F, Rosén A, Larkö O, Wennberg AM. Fluorescence contrast and threshold limit: implications for photodynamic diagnosis of basal cell carcinoma. *J. Photochem. Photobiol. B: Biol.* 2003; **69**: 121–127.
44. Scott MA, Hopper C, Sahota A, Springett R, McIlroy BW, Bown SG, MacRobert AJ. Fluorescence photodiagnostics and photobleaching studies of cancerous lesions using ratio imaging and spectroscopic techniques. *Lasers Med Sci* 2000; **15**: 63–72.

A non-probabilistic approach to blind decomposition of low-dimensional multi-spectral image is presented exploiting spectral diversity and spatial sparsity between the materials resident in the image. The unknown number of materials can be less than, equal to, or greater than the number of spectral bands and is estimated using the data clustering method. Materials are recovered by a multilayer hierarchical alternating least square nonnegative matrix factorization algorithm that showed best performance in comparison with methods based on $\ell 1$-norm minimization: linear programming and interior-point methods.

I. Kopriva* and A. Cichocki . . . . . xx–xx

Blind decomposition of low-dimensional multi-spectral image by sparse component analysis